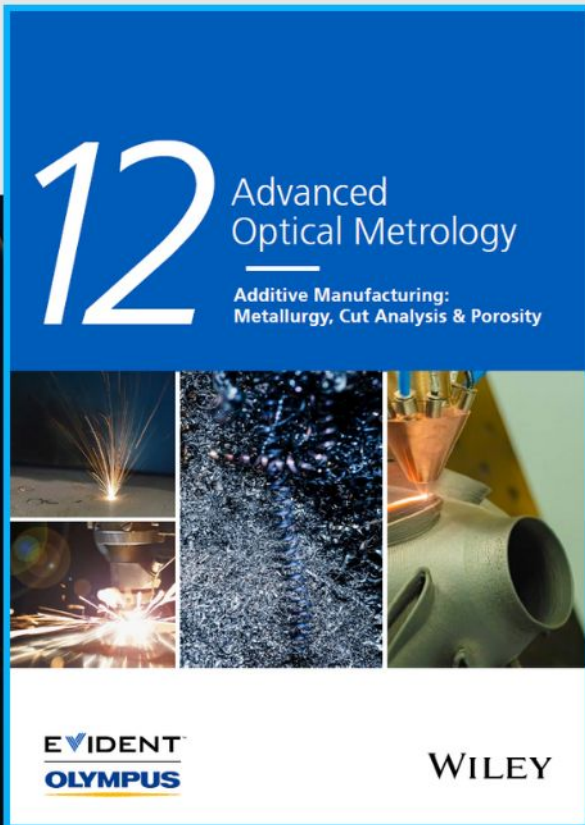




Additive Manufacturing: Metallurgy, Cut Analysis & Porosity



The latest eBook from
Advanced Optical Metrology.
Download for free.

In industry, sector after sector is moving away from conventional production methods to additive manufacturing, a technology that has been recommended for substantial research investment.

Download the latest eBook to read about the applications, trends, opportunities, and challenges around this process, and how it has been adapted to different industrial sectors.

EVIDENT™
OLYMPUS

WILEY

3D Chiral MetaCrystals

Marco Esposito,* Mariachiara Manoccio, Angelo Leo, Massimo Cuscunà, Yali Sun, Eduard Ageev, Dmitry Zuev,* Alessio Benedetti, Iolena Tarantini, Adriana Passaseo, and Vittorianna Tasco*

Fine control of the chiral light–matter interaction at the nanoscale, by exploiting designed metamaterial architecture, represents a cutting-edge craft in the field of biosensing, quantum, and classic nanophotonics. Recently, artificially engineered 3D nanohelices demonstrate programmable wide chiroptical properties by tuning materials and architecture, but fundamental diffractive aspects that are at the origin of chiral resonances still remain elusive. Here, a novel concept of a 3D chiral metacrystal, where the chiroptical properties are finely tuned by in-plane and out-of-plane diffractive coupling, is proposed. Different chiral dipolar modes can be excited along the helix arms, generating far field optical resonances and radiation pattern with in-plane side lobes, and suggesting that a combination of efficient dipole excitation and diffractive coupling matching controls the collective oscillations among the neighbor helices. The proposed concept of compact chiral metacrystal can be suitable for integration with quantum emitters and open perspectives in novel schemes of enantiomeric detection.

1. Introduction

The continuously-growing interest toward metamaterials' development comes from the possibility to enable non-naturally occurring optical properties.^[1,2] In the last years, metamaterials have been realized exploiting different materials, shapes,

layouts, and dimensions to exhibit functional and exotic optical properties in various operational regions, from infrared to visible, for several applications of technological interest.^[3–5]

Fundamentally, the optical response of a metamaterial is tailored by the interplay between constitutive material and geometric architecture. When the basic building block possesses parity inversion due to a swirling shape, chiral metamaterials^[6–9] could be built, and they exhibit anisotropic behavior when interacting with circularly polarized light (CPL). In this frame, chiroptical properties such as circular dichroism (CD) and optical rotation can reach higher orders of magnitude than that observed in naturally occurring chiral molecules,^[10,11] and, consequently, are of potential interest in many application


fields, such as biosensing and chemistry.^[12–15] In particular, chiral metamaterials can work as ideal photonic elements, such as compact alternatives to bulky systems for light polarization handling, and can complement photonics integrated circuits.^[16–19]

The most intuitive and intrinsically chiral shape is the helix geometry. Previous studies on metallic nano- and micro-helices have shown how the far field optical resonances and the related radiation pattern depend on the interplay between structural sizes and inspecting light wavelength and polarization.^[20–22] The possibility to get large chiroptical effects from this family of metamaterial has been demonstrated.^[23–25] We also know that a fundamental chiral meta-atom can be identified as the smallest helix segment exhibiting non-zero chiroptical effects within a certain spectral range.^[26] A further step in such a technology can be the 3D ordering of helix-shape nanostructures, with designed structure and periodicities, to simultaneously control the degree of far field coupling with incident light in the forward direction, and the interference among scattered fields from neighboring helices, as a function of circular polarization. This can lead to chiral metacrystals (CMC), that is, 3D arrangements of chiral meta-atoms, as a novel class of optical components, with circular polarization-dependent diffractive coupling, driven by both the out-of-plane and the in-plane parameters of the crystal. Such a spectral and polarization engineering, not achievable at the single nanoparticle level,^[27] is suitable for easy implementation in compact photonic systems and components, preferably working under normal incidence excitation. On the other hand, a full and effective control on both the CMC rulers (in-plane and out-of-plane lattice constants) poses significant

M. Esposito, M. Manoccio, A. Leo, M. Cuscunà, A. Passaseo, V. Tasco
CNR NANOTEC Institute of Nanotechnology
Via Monteroni, Lecce 73100, Italy
E-mail: marco.esposito@nanotec.cnr.it; vittorianna.tasco@nanotec.cnr.it
Y. Sun, E. Ageev, D. Zuev
School of Physics and Engineering
ITMO University
49 Kronverkskiy av., St. Petersburg 197101, Russia
E-mail: d.zuev@metalab.ifmo.ru

A. Benedetti
D.I.E.T. Department
“Sapienza: Università di Roma”
Via Eudossiana 18, Rome I-00184, Italy

I. Tarantini
Department of Mathematics and Physics Ennio De Giorgi
University of Salento
Via Arnesano, Lecce 73100, Italy

 The ORCID identification number(s) for the author(s) of this article can be found under <https://doi.org/10.1002/adfm.202109258>.

© 2021 The Authors. Advanced Functional Materials published by Wiley-VCH GmbH. This is an open access article under the terms of the Creative Commons Attribution License, which permits use, distribution and reproduction in any medium, provided the original work is properly cited.

DOI: 10.1002/adfm.202109258

technological challenges, particularly at VIS frequencies. A limited number of nanofabrication techniques offer complete flexibility toward such a multidimensional level of engineering. Even though in the last years, helix nanostructures have been demonstrated with high precision and accuracy by DNA-assisted synthesis,^[28,29] by glancing angle deposition,^[23,30,31] and by focused ion/electron beam processing,^[32,33] the deterministic construction of a helix-based CMC requires simultaneous control over 3D parameters and over the high precision positioning of seeding points, hardly achievable with most of the available techniques.^[30]

In the present work, we experimentally demonstrate the concept of CMC composed by metallic nanohelices. We first unveil the physical origin of the optical resonances at the single particle level, leveraged by the out-of-plane lattice constant, by combining numerical studies, based on finite difference time domain tools and realistic material parameters, with far field characterization. Then, we focus on the evolution from single element to collective behavior, taking into account the radiation pattern to estimate and understand mutual helix interaction. Such a thorough investigation is needed to finely engineer the diffractive coupling regime, along the in-plane and out-of-plane directions, and to achieve unprecedented control over the circular polarization discrimination exhibited by the CMC through its 3D lattice parameters, flexibly controlled by the employed focused ion beam processing.

2. Results and Discussion

The CMC concept underlying this work is schematically shown in **Figure 1**. The building blocks are metallic nanowires of diameter 120 nm, wound along the vertical direction to create single loop nanohelices, thus consisting of two chiral meta-atoms.^[26] In our study, the helix vertical pitch (VP) and length have been varied to get resonant behavior throughout the visible range as an effect of circular polarized light (CPL) excitation (**Figure 1a**).^[9,26,34] Moreover, to achieve efficient CP discrimination of transmitted light in the VIS under normal

incidence, it is desirable that each helix mainly works in axial mode, and also that collective behavior can be exploited and engineered.^[35] Therefore, following RF antenna theory^[36,37] and its extension to diffractively coupled helices,^[22] we engineered single helix geometry by choosing an external diameter (ED) of 300 nm, in order to have maximum efficiency radiating along the vertical axis, but with secondary components also radiating in the helix plane. This translates into a “quasi axial” radiation pattern, as schematically shown in **Figure 1b**: with such a design criterion, secondary side lobes of single helix radiation pattern appear, and their spatial extension, in the hundred nm range, can control the mutual far field interaction between helices. Therefore, if the designed chiral elements are arranged in a squared array (**Figure 1c**), to build up a diamond-structured crystal,^[38,39] the in-plane lattice parameter (LP), represented by the center-to-center distance among helices, can be chosen to enable diffractive coupling and far field interaction also between the single resonant helices.

The first step of our analysis was a thorough investigation of the single helix far field response. We focused on the scattering behavior, as a function of circular polarization for different out-of-plane lattice parameters (VP), as shown in **Figure 2a**, fabricated by focused ion beam induced deposition (FIBID) on ITO/glass substrate (details in the Experimental Section). Couples of single enantiomers (right-handed RH and left-handed LH, respectively) with identical geometry and composition were realized. Here, a RH structure is considered, with VP varied to keep a ratio with the excitation wavelength close to 1 (VP = 350, 550, and 800 nm);^[22] the total length of the nanowire, $l = \sqrt{(\pi * ED)^2 + VP^2}$, doesn't exceed 1.2 micron in the considered structures. Therefore, according to previous theories,^[20,40] it is reasonable to assess that the far field response of the single elements can exhibit eigenmodes in the visible spectral range, taking into account the plasmonic losses and the material behavior associated with the realistic dispersion of the platinum–carbon mixture constitutive medium, as commonly obtained with FIBID technology.^[41]

The numerical calculations of **Figure 2b** were performed by finite element method (FEM) approach (see the Experimental

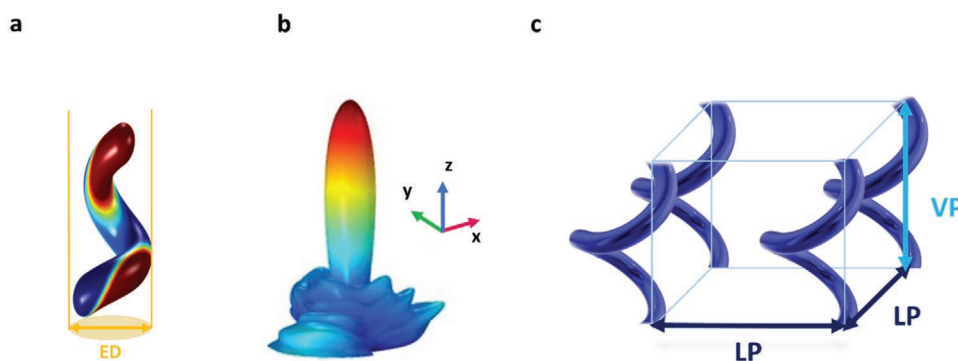


Figure 1. Schematic of the CMC concept. a) The unit cell consists of a metallic helix identified by the external diameter (ED) and the vertical pitch (VP). The spectral response of the single metallic element depends on the number of dipoles excited by inspecting light at a specific wavelength.^[20] b) The relationship between ED and inspecting wavelength determines the axial or radial operation of the antenna element. With a chosen ED of 300 nm, in the VIS range, our helices work in a “quasi-axial” scattering regime,^[36] as schematically shown by the qualitative radiation pattern. Such a radiation profile allows for efficient transmission from the single element along the forward direction, with an additional in-plane component enabling collective interaction from the array. c) Center-to-center distance among the helices (lattice parameter LP) represents the in-plane lattice parameter of the complete CMC.

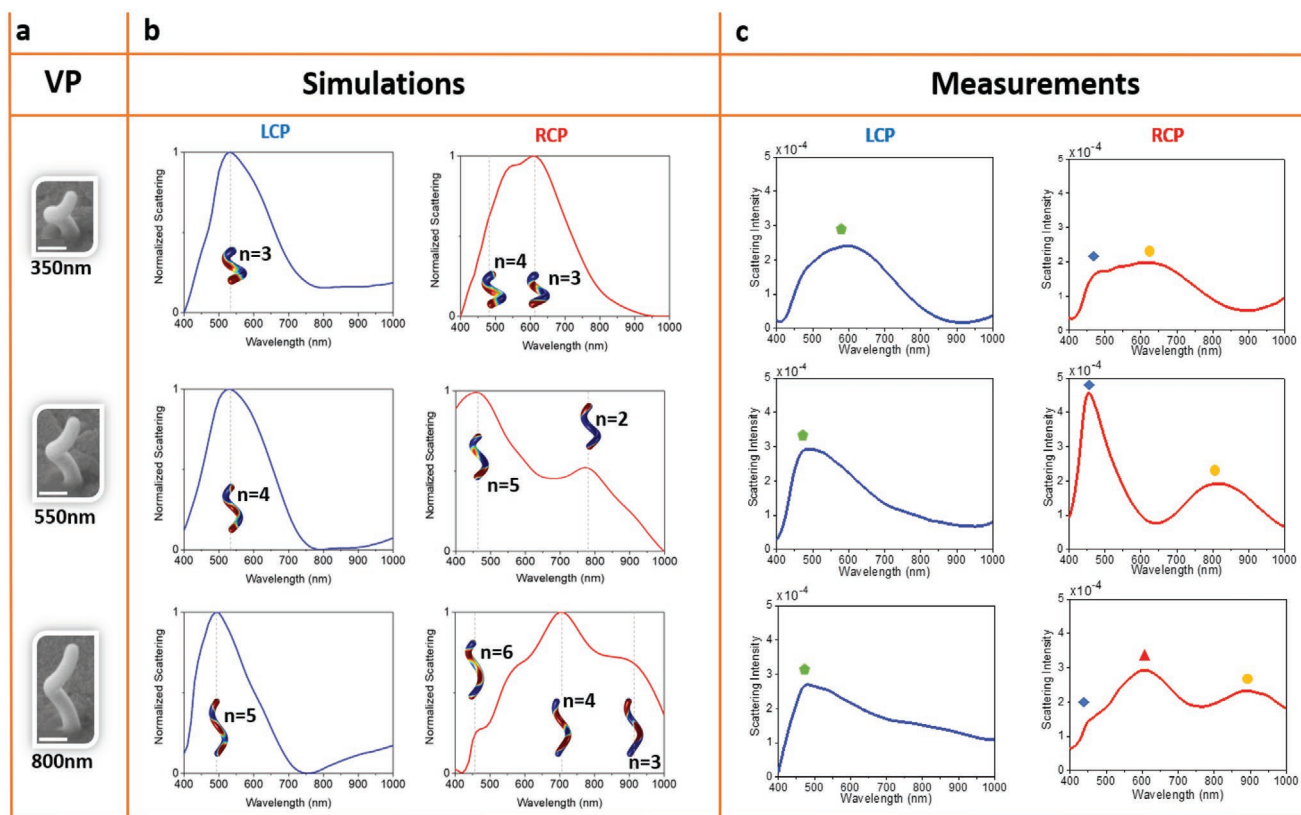


Figure 2. Numerical and experimental scattering behavior of single helices as a function of VP (350, 550, and 800 nm), and circularly polarized incident light. a) SEM images of single helices with different VPs; scale bar is 200 nm. b) Numerically simulated normalized scattering spectra: the dashed grey lines highlight the resonance peaks where we have calculated the electric field distribution on the helix surface to find the associated dipoles number as a function of the incident light polarization. c) Measured scattering spectra in arbitrary units of single helices: the colored symbols identify the wavelength position of the main resonances as a function of VP, and for both the light circular polarizations. In particular, the LCP resonance is not affected by the VP variation; conversely, for the RCP case, while the resonance for high dipole number (blue rhomb) remains in the initial position, the peak corresponding to low dipole number resonance (yellow circle) shifts toward lower frequency when the VP increases, unveiling the presence of another resonance corresponding to an intermediate dipole number (red triangle).

Section for further details), and the scattering spectra were normalized to their maxima, considering the experimental set-up described below. First of all, they show that, when incident light is left circularly polarized (LCP), that is, opposite to structure handedness (RH in our case), the scattering resonances are not strongly influenced by the structure length (i.e., by VP, Figure 2b, left panel). The response appears as a broad peak centered at ≈ 500 nm, without substantial changes in position and modal linewidth within the VP investigated range. Moreover, as shown by the calculated electric field distribution along the helix surface, these transitions can be related to the excitation of electric dipoles, increasing in number with VP (from $n = 3$ to $n = 5$).

On the other hand, when incident CPL is switched to RCP (Figure 2b, right panel), thus matching the structure handedness (RH), the effect of VP becomes more significant, with the appearance in the whole spectrum of additional resonances, which were not present in the previous cases.

Coupling and hybridization among the different dipoles can arise, governed by the distance between dipoles, that, in turn, can be set acting on VP.^[42] For small VP (350 nm), the plasmonic dipoles belong to continuous arms which are close to

each other, and this can lead to vertical dipole coupling and to spectrally broad resonance. It is also intuitive that, in this case, the spectral responses under RCP and LCP excitation, respectively, are very similar to each other, because the geometrical chirality is weak, and the helix approaches an achiral hollow cylinder. As VP increases to 550 nm, the two CPLs can clearly excite different modes associated to a different dipole number. In particular, the RCP scattering spectrum exhibits additional and redshifted peaks, where the peak with the lowest number of dipoles corresponds to the mode at longer wavelengths, while the highest order continues to match the resonance generated by opposite handedness exciting light (LCP light). Moreover, the mutual interactions between adjacent helix arms are reduced here, given the increased distance among them. All these features lead to the onset of well-defined resonances in the RCP case and to multiple bands of circular polarization discrimination.

When the height is increased up to 800 nm, the plasmonic resonances corresponding to the low dipole number are further redshifted, clearly unveiling the excited optical resonances corresponding to the high dipole number. Interaction between arms is further reduced here, as well as the related plasmonic

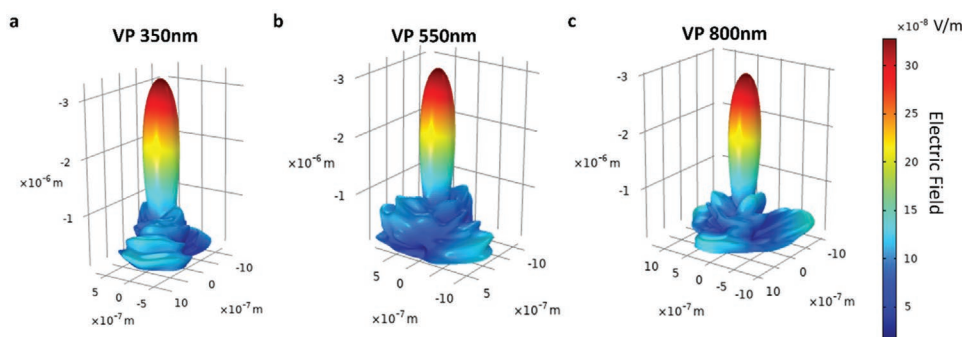


Figure 3. Calculated radiation pattern of single nanohelix for RCP incident light at 490 nm with VP of: a) 350 nm, b) 550 nm, and c) 800 nm. In all cases, a quasi-axial pattern is exhibited, but the side lobe extension progressively increases with VP.

noise due to the stacked dipole weak coupling. The helix is stretched along the vertical axis for the VP increment, thus approaching the other extreme achiral case of a 3D nanopillar. Consequently, the CPL discrimination is again reduced in such a condition.

Scattering measurements were performed at the single RH particle level for each VP, as a function of circular polarization (Figure 2c). The circular scattering spectra were collected with a multifunctional confocal setup (see the Experimental Section for details). The configuration of the setup allowed to measure all optical signals from a single nanoparticle, when interparticle distance was larger than 1 μm . For the dark field measurements, the single helix nanostructure is illuminated by LCP/RCP light with an oblique incidence angle of 67°. In this case, by placing an objective with numerical aperture around 0.5 above the top of the sample, the reflected beam of the primary light is out of the focus of the objective. Thus, only the pure scattering signal is collected from the top objective. Such configuration is different from a dark field scheme with condenser applied for the helix nanostructure measurements reported in refs. [21,43–45]. In our case, the utilized type of experimental scheme has no limitations related to the substrate transparency and allows to comprehensively study the scattering response even with azimuthal angle dependence.

Very good agreement is obtained with respect to numerical simulations discussed above, confirming that, when the incident light has the same handedness of the helix, the optical modes with low dipole number are more effectively excited. On the contrary, under the excitation of light with opposite handedness, the higher dipole number modes are more efficiently excited, while low frequency dipoles are suppressed. As observed in the optical response of other plasmonic chiral nanosystems,^[20,46,47] the excitation efficiency of different optical resonances is maximized when the incident field exhibits a spatial distribution similar to the arrangement of the plasmonic dipoles along the nanostructure. In agreement with this model, in our system, for the nanohelix with VP = 550 nm, considering the matching case between the handedness of the structure and that one of the incident light, we can infer that the RCP field efficiently excites the modes with $n = 2$ and $n = 5$. On the other hand, the LCP field matches the mode pattern just for $n = 4$ on the helix surface. This behavior is in line with the calculated trends of transferred extinction power^[20] for different CP light reported in Figure S4, Supporting Information.

Measurements also quantitatively confirm that the most pronounced CP discrimination occurs for VP of ≈ 550 nm, where scattered intensity of RCP light is nearly doubled as compared to LCP. Furthermore, as a confirmation for fabrication and measurement reliability, the spectra in Figure S1a,b,c, Supporting Information, show that LH enantiomers exhibit exactly the opposite chiral scattering responses as compared to RH enantiomers. On the other hand, absence of chiroptical effects is observed in the length/dependent scattering spectra of achiral nanopillars (Figure S1d, Supporting Information), grown under the same conditions of helices, with the same helix composition and wire diameter.

Therefore, the effective dipolar length and the excitable resonant modes can be finely tuned by varying the helix VP parameter, as experimentally feasible with the growth technique exploited for this work, and this, in turn, controls the coupling with the circularly polarized incident light.

Within a periodic array and under normally-incident light, the coupling between adjacent helices, driven by their mutual distance, is expected to result in a frequency shift of the dipolar resonances, along with enhanced scattering and stronger effective damping.^[48] However, it must be considered that the out-of-plane helix parameter investigated above, rules out not only the far field optical resonances of the nanostructures, but also the features of the helix radiation pattern. Numerical calculations reported in **Figure 3** show that, while a quasi-axial radiation pattern is exhibited by the single element for all the investigated VPs, for small VP, the side lobes can be more tightly confined around the nanostructures (within ≈ 500 nm), while they gradually extend up to ≈ 1 micron along the substrate plane as VP increases. Consequently, the possibility to deterministically and uniformly replicate the helix geometry throughout a designed array, can allow to further engineer collective interactions via multiple scattering, and realize a CMC, capable to work as a compact and miniaturized polarization control element, potentially integrable within a photonic circuit. It is worth noting that FIB processing, as long as proper calibration steps and pressure stability controls are performed, has demonstrated to be an additive manufacturing solution appropriate to grow large area arrays of complex nano-objects with extremely high reproducibility.^[49] Even though further improvements are needed with respect to scalability and time consumption,^[32] computer aided designs and manufacturing systems ensure reliable multiple element growth in reasonable times. The technique can

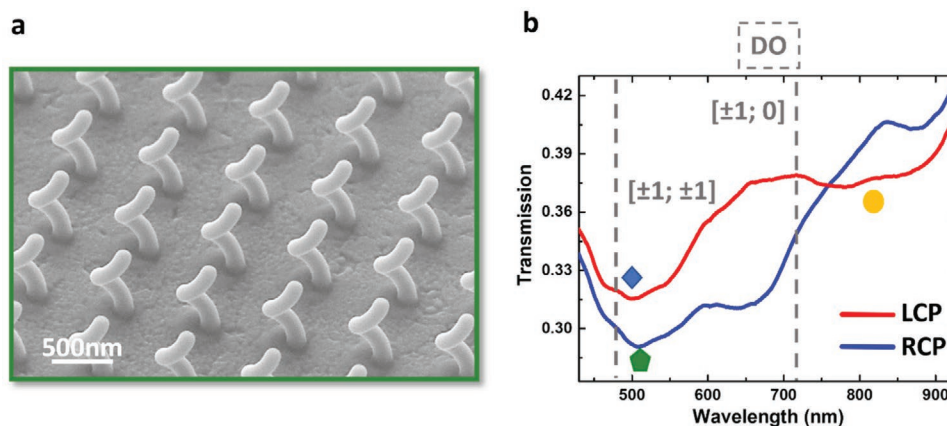


Figure 4. a) SEM view of the CMC with VP = 550 nm and wide LP = 700 nm, in order to reduce mutual helix interaction. b) Transmission measurements as a function of CPL for the same array, showing minima (same symbols as in Figure 2) corresponding to the dipolar resonances highlighted by scattering experiments, and additional modulations which can be inferred to lattice effects (diffractive orders, DO ($\pm 1; 0$) and ($\pm 1; \pm 1$)).

allocate complex 3D structures as close as few hundreds of nm, being intrinsically limited only by the wire diameter and by the beam probe size. Therefore, collective interactions between neighboring helices can be effectively engineered, even in a closely coupled regime where scattered fields from a single element can constructively interfere.

A first insight into the collective behavior can be gained when right-handed nanohelices are periodically arrayed with an in-plane parameter of 700 nm (Figure 4a), that allows neglectable interaction among the helices, given the side lobes extension of the radiation pattern for a VP of 550 nm (Figure 3a). The measured transmission spectra from the whole array (see Experimental Section for further details) evidences the presence of optical resonances at the same low frequency and high frequency positions observed from single helix scattering, for any CP handedness (symbols in Figure 4b). The measurements also provide an insight into the lossy behavior of our nanostructures, induced by the large absorption coefficient (k) of the Pt/C composite (Figure S2, Supporting Information), and contributing to the pronounced spectral broadening.^[50] Moreover, the effect of the ordered array is the appearance of additional modulations at wavelengths corresponding to diffractive orders (DO) of the squared array (in particular ($\pm 1; 0$) and ($\pm 1; \pm 1$)), suggesting the possibility to overlap them with the nanostructure resonances toward more complex hybrid states.^[51,52] If the lattice is shrunk down to LP lower than 700 nm, the mutual scattering among close elements is expected to be enhanced.

We analyze the results of these effects in the dissymmetry factor (g)^[20] of Figure 5, as directly calculated through the normalized difference between the RCP and LCP transmitted light (shown in Section S3, Supporting Information) through the arrays, as follows:

$$g = \frac{2(I_{LCP} - I_{RCP})}{(I_{RCP} + I_{LCP})} \quad (1)$$

The g -factor plots show a general redshift with the increase of the crystal constants, more pronounced for LP than for VP. In a first approximation, we can assimilate the helix to a multi-stack of split ring resonators (SRRs) and discuss our LP-dependent

results in comparison with previous work on arrayed SRRs^[53] with geometrical parameters similar to our helices, and excited upon oblique incidence. In that case, for a squared array under linear polarizations, in-plane electric dipole coupling and out-of-plane magnetic dipole coupling were responsible of the redshifts and blueshifts of the transmission resonances when LP is varied, as strong near-field electrostatic and magnetostatic dipole couplings were induced. In our case, by putting the helices in strong proximity (reduced LP value of 435 nm), the total system energy seems to decrease, given the blue-shifted transmission valleys (Figure S3, Supporting Information) and related dichroic band extremes and null point NP (Figure 5a,b). In particular, the effect of lateral strong interactions among neighbor helices is evident on the short wavelength peak of the bi-signed spectrum. As also observed for arrayed SRRs, it is possible that enhanced scattering and effective super-radiant damping lead to a broadening and weakening of the resonances^[54] resulting in the strong reduction of the g -factor intensity for the short lattice period. On the other hand, a larger spacing between helices induces a spectral redshift which can be ascribed to the magnetic and electric interactions decrement,^[48] along with a g -factor intensity drop as a consequence of the reduced dipole number per volume (Figure 4b). The observed results, as a function of in-plane lattice parameter, anticipate the possibility to excite 3D chiral surface lattice resonances in the VIS range, given that a proper optical impedance matching is realized between substrate and superstrate.^[55]

Finally, the VP was also finely tuned in the average LP array, within an extended range between 270 and 800 nm (Figure 5c; Figure S3, Supporting Information). We note that, for each VP, larger g -factor can be achieved in the blue part of the spectra and that, by increasing the VP value, the λ_g^{Peak} (both at short and long wavelength) red shifts (Figure 5d). The increment of dipolar length accompanied by the increase of scattered field side lobes, modulates the blue-band intensity, which first increases with VP, and afterward, drops down (Figure 5d), giving an optimal intensity value of ≈ 0.24 for VP in the range between 450 and 500 nm.

This analysis demonstrates the existence of a small range of VP values that maximizes the chiroptical properties of the

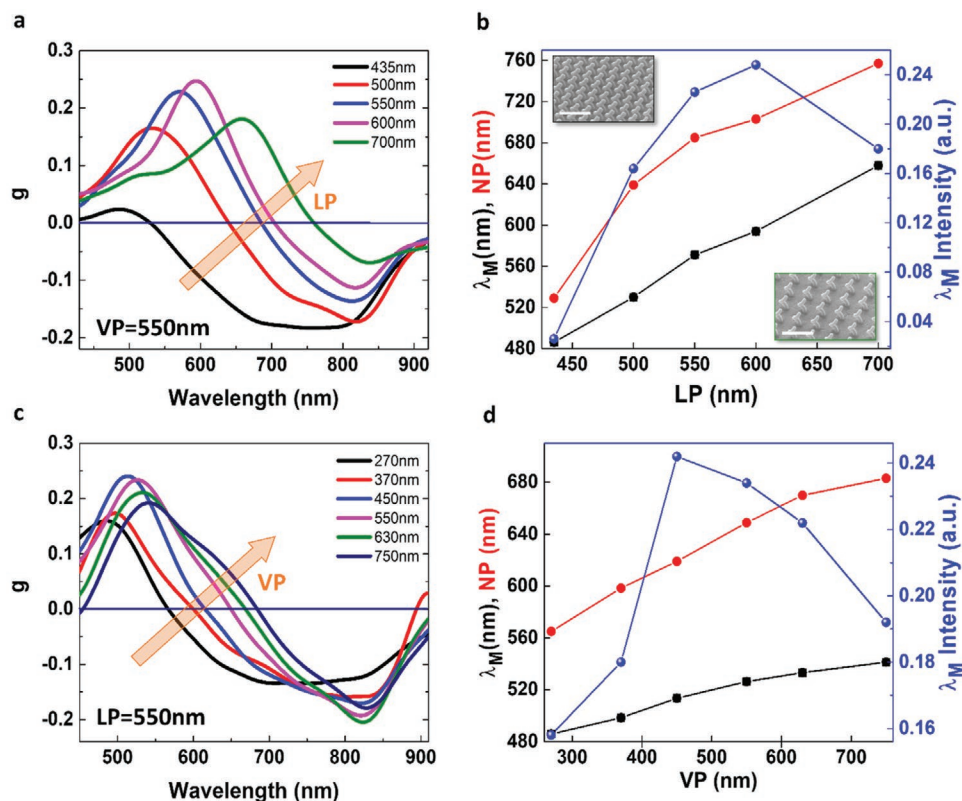


Figure 5. a) g -factor calculated from the measured transmission spectra of the fabricated CMC with VP fixed at 550 nm and tuning LP. b) Related maximum peak wavelengths (λ_M , black symbols) and intensities (blue symbols), along with g -factor null points (NP, red dots). c) g -factor calculated from the measured transmission spectra of the fabricated CMC with LP fixed at 550 nm and tuning VP. d) Related maximum peak wavelengths (λ_M , black symbols) and intensities (blue symbols), along with g -factor null points (NP, red dots).

plasmonic helical systems in the visible range. Out of this range, the structures degenerate toward achiral configurations, which can be the opposite cases of hollow cylinder or pillar.

3. Conclusions

To conclude, we have proposed a novel concept of 3D CMC, consisting of nanohelix-shaped metamaterials, with chiroptical properties finely engineered through the in-plane and out-of-plane diffractive coupling. We have shown that under circularly polarized light, different dipolar modes can be excited along the helix arms, depending on the polarization handedness, and on the out-of-plane crystal lattice constant. These modes are the origin of far field optical resonances and of radiation pattern with in-plane extending side lobes. This understanding suggests that collective oscillations between the neighbor helices can be controlled, not only by their mutual distance, but also thanks to a combination of efficient dipole excitation and diffractive coupling matching, allowing to optimize and maximize the overall chiroptical response of the CMC. The tunability of optical response in a broadband spectral range, and the flexibility of the fabrication process make the CMC a promising platform for creation of miniaturized circular polarizers for photonic circuits^[56] which are potential candidates for a wide set of applications, from

optoelectronic devices^[57] and displays, to integrated quantum chips and biosensors.^[15]

In particular, given the large chiroptical effects and the metallic nature of the system, novel applications in the emerging field of plasmon-driven chemical reactions,^[58] involving asymmetric synthesis, as well as in extremely high sensitivity biomolecular detection, can be envisioned.^[14]

4. Experimental Section

Sample Fabrication: The samples had been grown on an ITO-on-glass substrate by means of focused ion beam induced deposition technique, by employing a Carl Zeiss Auriga40 Crossbeam FIB/SEM system coupled with a gas injection system (GIS), aligned with respect to the upper side of the deposition area, while trimethyl(methylcyclopentadienyl)platinum(IV) had been used as gaseous precursor.

When the ion beam interacted with the substrate, it broke the gas molecules of the precursor locally injected through the nozzle. The initial layout, consisting of an empty circle, was set in the Raith Elphy Multibeam pattern generator, which also controlled the exposure parameters of the beam. The evolution along the third dimension was ruled by setting the beam energy at 30 keV, the beam current at 1 pA, and the step size, which controls the overlapping of the nucleation sites, at 10 nm. To increase the size of VP for each studied array, the dwell time was progressively increased from 120 to 320 ms. During the process, the chamber pressure was kept between 8×10^{-7} and 1.06×10^{-6} mbar. For the realization of the arrays, the distance among the helices was set

in the pattern generator. However, during the array fabrication processing, the proximity effects and the local pressure variations affected the amount of the deposited material, especially in the case of large arrays as in the studied case. Therefore, to optimize the flow conditions, a dose compensation protocol to overcome the proximity effects issues^[41] was applied together with a proper positioning of the GIS at 100 μm from the writing zone, and the needle with a tilt angle of 70° with respect to the substrate. Finally, to restore the pressure in the chamber, a refresh time of 5 min was applied among the growth of 20 elements.

SEM characterization of the single nano-helices and of the arrays was performed by means of a Merlin Zeiss microscope operating in scanning mode.

Optical Characterization: Transmission spectra were recorded by using an optical microscope Zeiss Axioscope A1 with a home-made confocal system. The sample was back-illuminated with a tungsten lamp, focalized with a condenser with NA < 0.1. Then, the transmitted light was collected using a 40 \times objective lens with NA < 0.95. Subsequently, the light was guided through a three lenses system to reconstruct, collimate, and refocus the image in the real space. Finally, the light was directed to a CCD camera (Hamamatsu Orca R2) coupled with a 200 mm spectrometer. The real image could be spatially selected with adjustable square slits. The circularly polarized light had been produced using a linear polarizer (Carl Zeiss, 400–800 nm) and a superachromatic waveplate (Carl Zeiss, 400–800 nm). The transmission measurements were normalized to the optical response of the substrate. The scattering measurements of the single chiral nanostructure were carried out with a non-polarized light from halogen lamp passing through a Glan linear polarizer and then through a superachromatic quarter waveplate to generate circularly polarized light. Then, the light was focused into the sample by a Mututoyo Plan Apo NIR Objective (M = 10 \times , NA = 0.26). The oblique incident angle was set at 67° to eliminate the reflection beam from the collecting channel. The scattered light was collected by a Mututoyo Plan Apo NIR Objective (M = 50 \times , NA = 0.42) from the top of the sample and then directed to the spectrometer. The distance between single helices was designed to be more than 10 μm ; in this case, the top objective could only capture the scattering signal coming from the selected single plasmonic helix.

Numerical Simulations: Numerical simulations were performed by exploiting the wave optics module of COMSOL Multiphysics 5.5, by carrying out a frequency domain study of electromagnetic waves propagating among the mere nanostructures, the surrounding medium, and perfectly matched layer, on which settings were scattering boundary conditions. Here, the scattered wave was considered plane at first order. For far field calculations, the domain was the air surrounding the single helix. The material dispersions used for platinum/carbon alloy were from ref. [6]. According to the experimental setup, the structure was excited by a circular polarized plane waves source with azimuthal angle of 60° and placed at enough distance from the investigated structure. The scattered signal was collected through an opening of 30° amplitude with respect to the zenith. Wavelength sweeping was performed in a range between 400 and 1000 nm with a step of 10 nm, leading to define far field radiation patterns and charge density distribution on the structure surface. The extinction spectra were obtained by comparison among numerical simulations of scattering from structures and dark response ones.

Supporting Information

Supporting Information is available from the Wiley Online Library or from the author.

Acknowledgements

M.E. and M.M. contributed equally to his work. This work was supported by “Tecnopolo per la medicina di precisione” (TecnoMed Puglia) – Regione

Puglia: DGR no. 2117 del 21/11/2018 CUP: B84118000540002. V.T. is thankful for the Short Term Mobility program of CNR. This work is supported by the Ministry of Science and Higher Education of the Russian Federation, Project 13.2251.21.0110, and by a grant from the Italian Ministry of Foreign Affairs and International Cooperation (RU21GR06, CUP B55F21005980001).

Open access funding provided by Consiglio Nazionale delle Ricerche within the CRUI-CARE agreement.

Conflict of Interest

The authors declare no conflict of interest.

Data Availability Statement

Research data are not shared.

Keywords

chirality, chiral photonics, chiral plasmonics, circular dichroism, focused ion beam induced deposition

Received: September 13, 2021

Revised: November 4, 2021

Published online: December 1, 2021

- [1] H.-T. Chen, A. J. Taylor, N. Yu, *Rep. Prog. Phys.* **2016**, 79, 076401.
- [2] W. T. Chen, A. Y. Zhu, F. Capasso, *Nat. Rev. Mater.* **2020**, 5, 604.
- [3] S. Lee, S. Baek, T.-T. Kim, H. Cho, S. Lee, J.-H. Kang, B. Min, *Adv. Mater.* **2020**, 32, 2000250.
- [4] J. Qian, P. Gou, H. Pan, L. Zhu, Y. S. Gui, C.-M. Hu, Z. An, *Sci. Rep.* **2020**, 10, 19240.
- [5] S. Sharma, R. Kumari, S. K. Varshney, B. Lahiri, *Rev. Phys.* **2020**, 5, 100044.
- [6] M. Esposito, V. Tasco, F. Todisco, A. Benedetti, D. Sanvitto, A. Passaseo, *Adv. Opt. Mater.* **2014**, 2, 154.
- [7] J. Kaschke, M. Wegener, *Nanophotonics* **2016**, 5, 510.
- [8] Y. Zhao, M. A. Belkin, A. Alù, *Nat. Commun.* **2012**, 3, 870.
- [9] Y. Guan, Z. Wang, B. Ai, C. Chen, W. Zhang, Y. Wang, G. Zhang, *ACS Appl. Mater. Interfaces* **2020**, 12, 50192.
- [10] L. D. Barron, in *Chirality at the Nanoscale: Nanoparticles, Surfaces, Materials and More*, 1st ed. (Ed: D. B. Amabilino), Wiley-VCH, Weinheim, Germany **2009**, pp. 1–29.
- [11] J. L. Greenfield, J. Wade, J. R. Brandt, X. Shi, T. J. Penfold, M. J. Fuchter, *Chem. Sci.* **2021**, 12, 8589.
- [12] E. Hendry, T. Carpy, J. Johnston, M. Popland, R. V. Mikhaylovskiy, A. J. Laphorn, S. M. Kelly, L. D. Barron, N. Gadegaard, M. Kadodwala, *Nat. Nanotechnol.* **2010**, 5, 783.
- [13] X. Wei, J. Liu, G.-J. Xia, J. Deng, P. Sun, J. J. Chruma, W. Wu, C. Yang, Y.-G. Wang, Z. Huang, *Nat. Chem.* **2020**, 12, 551.
- [14] M. Manocchio, M. Esposito, E. Primiceri, A. Leo, V. Tasco, M. Cuscunà, D. Zuev, Y. Sun, G. Maruccio, A. Romano, A. Quattrini, G. Gigli, A. Passaseo, *Nano Lett.* **2021**, 21, 6179.
- [15] Y. Zhao, A. N. Askarpour, L. Sun, J. Shi, X. Li, A. Alù, *Nat. Commun.* **2017**, 8, 6.
- [16] M. Wang, R. Salut, H. Lu, M. A. Suarez, N. Martin, T. Grosjean, *Light Sci. Appl.* **2019**, 8, 76.
- [17] M. Wang, Z. Huang, R. Salut, M. A. Suarez, H. Lu, N. Martin, T. Grosjean, *Nano Lett.* **2021**, 21, 3410.

- [18] M. D. Turner, M. Saba, Q. Zhang, B. P. Cumming, G. E. Schröder-Turk, M. Gu, *Nat. Photonics* **2013**, *7*, 801.
- [19] M. Cuscunà, M. Manoccio, M. Esposito, M. Scuderi, G. Nicotra, I. Tarantini, A. Melcarne, V. Tasco, M. Losurdo, A. Passaseo, *Mater. Horiz.* **2021**, *8*, 187.
- [20] K. Höflich, T. Feichtner, E. Hansjürgen, C. Haverkamp, H. Kollmann, C. Lienau, M. Silies, *Optica* **2019**, *6*, 1098.
- [21] P. Woźniak, I. De Leon, K. Höflich, C. Haverkamp, S. Christiansen, G. Leuchs, P. Banzer, *Opt. Express* **2018**, *26*, 19275.
- [22] R. Wang, C. Forestiere, L. Dal Negro, *Opt. Express* **2015**, *23*, 25496.
- [23] U. Kilic, M. Hilfiker, A. Ruder, R. Feder, E. Schubert, M. Schubert, C. Argyropoulos, *Adv. Funct. Mater.* **2021**, *31*, 2010329.
- [24] M. Schäferling, D. Dregely, M. Hentschel, H. Giessen, *Phys. Rev. X* **2012**, *2*, 031010.
- [25] J. K. Gansel, M. Thiel, M. S. Rill, M. Decker, K. Bade, V. Saile, G. von Freymann, S. Linden, M. Wegener, *Science* **2009**, *325*, 1513.
- [26] M. Esposito, V. Tasco, F. Todisco, M. Cuscunà, A. Benedetti, M. Scuderi, G. Nicotra, A. Passaseo, *Nano Lett.* **2016**, *16*, 5823.
- [27] S. Kim, C. Y. Zheng, G. C. Schatz, K. Aydin, K.-H. Kim, C. A. Mirkin, *Nano Lett.* **2020**, *20*, 8096.
- [28] A. Kuzyk, R. Schreiber, Z. Fan, G. Pardatscher, E. M. Roller, A. Högele, F. C. Simmel, A. O. Govorov, T. Liedl, *Nature* **2012**, *483*, 311.
- [29] X. Shen, A. Asenjo-Garcia, Q. Liu, Q. Jiang, F. J. Garcia de Abajo, N. Liu, B. Ding, *Nano Lett.* **2013**, *13*, 2128.
- [30] J. G. Gibbs, A. G. Mark, S. Eslami, P. Fischer, *Appl. Phys. Lett.* **2013**, *103*, 213101.
- [31] Z.-Y. Zhang, Y.-P. Zhao, *Appl. Phys. Lett.* **2007**, *90*, 221501.
- [32] M. Manoccio, M. Esposito, A. Passaseo, M. Cuscunà, V. Tasco, *Micromachines* **2021**, *12*, 6.
- [33] D. Kusters, A. De Hoogh, H. Zeijlemaker, H. Acar, N. Rotenberg, L. Kuipers, *ACS Photonics* **2017**, *4*, 1858.
- [34] M. Hentschel, M. Schäferling, X. Duan, H. Giessen, N. Liu, *Sci. Adv.* **2017**, *3*, e1602735.
- [35] M. Hentschel, D. Dregely, R. Vogelgesang, H. Giessen, N. Liu, *ACS Nano* **2011**, *5*, 2042.
- [36] C. A. Balanis, *Antenna Theory Analysis and Design*, 2nd ed., John Wiley & Sons, Inc., New York **1997**.
- [37] R. A. Smith, *Science* **1951**, *113*, 131.
- [38] A. Chutinan, S. Noda, *Phys. Rev. B* **1998**, *57*, R2006.
- [39] M. Maldovan, E. L. Thomas, *Nat. Mater.* **2004**, *3*, 593.
- [40] L. Novotny, *Phys. Rev. Lett.* **2007**, *98*, 266802.
- [41] A. Passaseo, G. Nicotra, A. Benedetti, M. Cuscunà, M. Scuderi, F. Todisco, V. Tasco, M. Esposito, *Nano Lett.* **2016**, *16*, 5823.
- [42] Y. Li, R. Ho, Y. Hung, *IEEE Photonics J.* **2013**, *5*, 2700510.
- [43] L.-Y. Wang, K. W. Smith, S. Dominguez-Medina, N. Moody, J. M. Olson, H. Zhang, W.-S. Chang, N. Kotov, S. Link, *ACS Photonics* **2015**, *2*, 1602.
- [44] N. R. Famularo, L. Kang, Z. Li, T. Zhao, K. L. Knappenberger, C. D. Keating, D. H. Werner, *J. Chem. Phys.* **2020**, *153*, 154702.
- [45] J. Karst, N. H. Cho, H. Kim, H. E. Lee, K. T. Nam, H. Giessen, M. Hentschel, *ACS Nano* **2019**, *13*, 8659.
- [46] X. Yin, M. Schäferling, B. Metzger, H. Giessen, *Nano Lett.* **2013**, *13*, 6238.
- [47] B. Frank, X. Yin, M. Schäferling, J. Zhao, S. M. Hein, P. V. Braun, H. Giessen, *ACS Nano* **2013**, *7*, 6321.
- [48] Y. R. Li, R. M. Ho, Y. C. Hung, *IEEE Photonics J.* **2013**, *5*, 2700510.
- [49] L. Hirt, A. Reiser, R. Spolenak, T. Zambelli, *Adv. Mater.* **2017**, *29*, 1604211.
- [50] S. Christiansen, G. Leuchs, P. Banzer, P. Woźniak, G. Brönstrup, K. Höflich, *Nanotechnology* **2015**, *27*, 025705.
- [51] V. G. Kravets, A. V. Kabashin, W. L. Barnes, A. N. Grigorenko, *Chem. Rev.* **2018**, *118*, 5912.
- [52] M. B. Ross, C. A. Mirkin, G. C. Schatz, *J. Phys. Chem. C* **2016**, *120*, 816.
- [53] I. Sersic, M. Frimmer, E. Verhagen, A. F. Koenderink, *Phys. Rev. Lett.* **2009**, *103*, 213902.
- [54] M. Decker, N. Feth, C. M. Soukoulis, S. Linden, M. Wegener, *Phys. Rev. B* **2011**, *84*, 85416.
- [55] E. S. A. Goerlitzer, R. Mohammadi, S. Nechayev, K. Volk, M. Rey, P. Banzer, M. Karg, N. Vogel, *Adv. Mater.* **2020**, *32*, 2001330.
- [56] K. Konishi, T. Kan, M. Kuwata-Gonokami, *J. Appl. Phys.* **2020**, *127*, 230902.
- [57] S. P. Rodrigues, S. Lan, L. Kang, Y. Cui, P. W. Panuski, S. Wang, A. M. Urbas, W. Cai, *Nat. Commun.* **2017**, *8*, 14602.
- [58] O. Guselnikova, G. Audran, J.-P. Joly, A. Trelin, E. V. Tretyakov, V. Svorcik, O. Lyutakov, S. R. A. Marque, P. Postnikov, *Chem. Sci.* **2021**, *12*, 4154.